

# A Quantum Algorithm for Solving the Advection Equation using Hamiltonian Simulation

Peter Brearley\* and Sylvain Laizet

*Department of Aeronautics, Imperial College London, London, United Kingdom.*

(Dated: December 15, 2023)

A quantum algorithm for solving the advection equation based on sparse Hamiltonian simulation is presented. The matrix arising from the finite difference discretisation with explicit Euler time integration is embedded within the Hamiltonian to advance the solution in time. The unitary operator embeds the matrix to a high accuracy regardless of the Hamiltonian evolution time, so a time step succeeds with a high probability and errors of the same order as the conventional Euler method. If postselection does fail, the enacted operation is close to the identity matrix, having a negligible impact on the quantum state and allowing the computation to continue. Qubit requirements grow logarithmically with the number of grid points  $N$  and gate requirements grow polynomially as  $\tilde{O}(N^{1/D} Dk/\epsilon)$  (suppressing polylogarithmic terms) in  $D$  dimensions with  $k$ -order spatial discretisation and allowable error  $\epsilon$ , yielding a significant polynomial speedup over the classical  $O(N^{(1+D)/D})$ . Statevector simulations of a scalar transported in a two-dimensional laminar channel flow with a combination of periodic and Dirichlet boundary conditions are presented as a proof of concept of the proposed approach.

## I. INTRODUCTION

Quantum computing is expected to bring a profound shift in our computational capability. Among the promising applications of quantum computers is solving large-scale partial differential equations (PDEs) more efficiently than classical computers. PDEs are ubiquitous across science and engineering and solving them currently occupies the majority of the world's high-performance computing resources. The development of efficient quantum algorithms is therefore of immense value and has attracted a large interdisciplinary research community, spurred on by the continuing advancements in quantum hardware [1, 2].

Quantum algorithms for solving PDEs can be delineated into two categories: fully quantum algorithms that implement quantum circuits to evolve the quantum state as described by the PDE of interest, and quantum-classical hybrid algorithms where a quantum computer is used for a specific task in a larger, classical computation. Fully quantum approaches generally excel at solving linear PDEs because quantum operators act linearly on quantum states, allowing algorithms based on the finite difference method (FDM) [3–6], the finite element method (FEM) [7, 8] and spectral methods [9] to be effectively represented quantum mechanically. Encoding the solution from  $N = 2^n$  grid points within the amplitudes  $\alpha_j$  of an  $n$ -qubit quantum state  $|\psi\rangle = \sum_{j=1}^N \alpha_j |j\rangle$  leads to an exponentially growing capacity to store information and an inherent quantum parallelism when processing it. Amplitude encoding does not allow for the inspection of the full solution as with classical methods, but rather the extraction of global statistics into the limited output space. This may be adequate for the engineer depending

on the context and make previously intractable problems tractable. Fully quantum approaches are not limited to linear PDEs as techniques have been proposed based on the derivation of the nonlinear Schrödinger equation using mean-field techniques [10] and Carleman linearisation [11] to tackle nonlinear PDEs, but these are generally limited to weakly nonlinear interactions. On the other hand, variational quantum algorithms (VQAs) [12] for solving optimisation problems have been used as the basis for hybrid algorithms that have demonstrated a greater capability of tackling nonlinear PDEs [13–15]. Kyriienko *et al.* [14] used a machine learning strategy where differentiable quantum circuits were trained to solve nonlinear differential equations. Jaksch *et al.* [15] extended a quantum algorithm for solving nonlinear problems [13] to fluid dynamics, evaluating cost functions from matrix product state representations of the flow [16] to obtain a polynomial upper bound on the depth of variational network. VQA-based algorithms are promising for gaining a quantum advantage on near-term hardware due to the shorter coherence times required [12].

Most quantum algorithms for solving linear PDEs have a quantum linear systems algorithm (QLSA) at their core [3, 5–9, 17–19] such as the HHL algorithm [20] or further optimisations thereof [21]. Clader *et al.* [7] developed a quantum algorithm using a QLSA to implement the FEM for solving Maxwell's equations, and this was further clarified and developed by Montanaro and Pallister [8]. Cao *et al.* [3], Wang *et al.* [5] and Childs *et al.* [6] in their respective studies optimised a quantum algorithm based on the FDM to solve the Poisson equation by expressing the PDE as a system of linear equations and solving with a QLSA.

Quantum algorithms that do not depend on a QLSA have also been suggested. Costa *et al.* [4] developed a quantum algorithm that evolves a quantum state according to the wave equation using Hamiltonian simulation without the need for a QLSA, aside from in the proposed

---

\* p.brearley@imperial.ac.uk

generation of the initial conditions. A practical implementation of this algorithm was then developed and analysed by Suau *et al.* [22], confirming that the gate requirements agreed with the theoretical complexity. In a different study, Budinski [23] proposed a quantum algorithm for the advection-diffusion equation centred around the lattice Boltzmann method (LBM) that tracks the evolution of particle distribution functions on a grid. The main challenge of implementing the nonunitary collision step of the LBM was achieved with a linear combination of unitaries method. Jin *et al.* [24–26] introduced a ‘Schrödingerisation’ method that maps linear PDEs to a higher-dimensional system of Schrödinger equations that can be solved using Hamiltonian simulation techniques. The absence of a quantum phase estimation step within the QLSA in these methods leads to favourable polylogarithmic scaling in the allowable error per time step using sparse Hamiltonian simulation algorithms [27], as opposed to the linear scaling from a QLSA [20].

In this paper, a quantum algorithm is presented that solves the advection equation using Hamiltonian simulation. The advection equation is a foundational linear PDE spanning multiple industries as it models the transport of a scalar quantity in advection-driven flows. Applications include the vast oceanic and atmospheric flows used in climate modelling or the heat exchangers that cool oil refineries, chemical processing plants and power stations. Hamiltonian simulation is used to advance the quantum state according to the FDM with explicit Euler time integration without the need for a QLSA. The explicit discretised PDE leads to a matrix  $A$  that can be multiplied by the solution vector  $\vec{\phi}_t$  to advance the solution in time, i.e.  $\vec{\phi}_{t+1} = A\vec{\phi}_t$ . Since  $A$  is nonunitary, it cannot be applied directly as an operator to a quantum state  $|\phi_t\rangle$ , so is embedded into a larger Hamiltonian simulation [27, 28].

The mathematical description of the algorithm is provided next, followed by analyses of the errors, time step success probability and the complexity in Sections III, IV and V respectively. Statevector simulations of the algorithm applied to a two-dimensional laminar channel flow problem are provided and analysed in Section VI and the paper is ended with concluding remarks in Section VII.

## II. THE ALGORITHM

The advection equation models the transport of a scalar in a fluid flow when the effects of diffusion are negligible. It is defined as

$$\frac{\partial \phi}{\partial t} + u_j \frac{\partial \phi}{\partial x_j} = 0 \quad (1)$$

where  $\phi$  represents the scalar field (e.g. temperature, concentration) and  $u_j$  is the  $j^{\text{th}}$  component of the advective velocity vector, where repeated indices invoke the summation convention. The equation can be discretised using

the FDM to express  $\nabla \phi$  in terms of  $\phi$  and the chosen spatial and temporal grid spacings  $\Delta x$  and  $\Delta t$ . Using first-order forward temporal discretisation and second-order central spatial discretisation, the advection equation in one dimension for a constant velocity  $u$  becomes

$$\frac{\phi_m^{t+1} - \phi_m^t}{\Delta t} + u \frac{\phi_{m+1}^t - \phi_{m-1}^t}{2\Delta x} = 0 \quad (2)$$

for spatial grid point  $m$  and temporal location  $t$ . Equation (2) can be solved for  $\phi_m^{t+1}$ , obtaining an equation to advance the solution in time. A vector  $\vec{\phi}_t = [\phi_0^t, \phi_1^t, \dots, \phi_N^t]$  can be constructed from  $\phi$  to write Eq. (2) as a matrix transformation:

$$\vec{\phi}_{t+1} = A\vec{\phi}_t \quad (3)$$

For the described one-dimensional advection equation discretised with a second-order FDM, the matrix  $A$  takes the form

$$A = \begin{bmatrix} 1 & -\frac{r}{2} & 0 & \frac{r}{2} \\ \frac{r}{2} & \ddots & \ddots & 0 \\ & \ddots & \ddots & \ddots \\ 0 & & \ddots & \ddots & -\frac{r}{2} \\ -\frac{r}{2} & 0 & & \frac{r}{2} & 1 \end{bmatrix} \quad (4)$$

considering simple periodic boundary treatment where the first and last grid points are adjacent, leading to entries in the top-right and bottom-left corners. The stability parameter  $r = u\Delta t/\Delta x$  is the Courant-Friedrichs-Lewy (CFL) number that must not exceed 1 to ensure numerical stability [29]. In practice and especially for explicit schemes, lower values of the order of 0.1 are required. The algorithm can be applied to problems with increased spatial dimensions  $D$  or order of spatial discretisation  $k$ , growing the sparsity of the matrix as  $s = 1 + Dk$  with FDM coefficients determined by  $k$ .

To enact this nonunitary matrix on a quantum state  $|\phi_t\rangle$ , the nonunitary embedding procedure described by Gingrich and Williams [28] is used. A Hamiltonian  $H$  is constructed from  $A$  in the form

$$H = \begin{bmatrix} 0 & iA \\ -iA^T & 0 \end{bmatrix} \quad (5)$$

where  $i$  is the imaginary unit. A quantum state is evolved according to  $H$  by the unitary operator

$$\begin{aligned} \Omega &= \exp(-iH\theta) \\ &= \exp\left(\begin{bmatrix} 0 & A\theta \\ -A^T\theta & 0 \end{bmatrix}\right) \end{aligned} \quad (6)$$

where  $\theta$  is the Hamiltonian evolution time. The exponential function produces a block matrix with the structure

$$\Omega = \begin{bmatrix} \tilde{I} & \tilde{A} \\ -(-1)^{i+j} \tilde{A} & \tilde{I} \end{bmatrix} \quad (7)$$

The operator  $\Omega$  applied to a solution register  $|\phi_t\rangle$  supplemented by an ancilla qubit initialised as  $|1\rangle$  therefore produces the state

$$\Omega|1\rangle|\phi_t\rangle = \tilde{A}|0\rangle|\phi_t\rangle + \tilde{I}|1\rangle|\phi_t\rangle \quad (8)$$

For the advection equation, the matrices  $\tilde{A}$  and  $\tilde{I}$  retain the relative structure of  $A$  and the identity matrix  $I$  respectively, and this is true even for large values of  $\theta$  ( $0 \leq \theta \leq \pi/2$ ). Hence, a subspace of the Hilbert space evolves as described by the advection equation. Postselecting the ancilla qubit in the state  $|0\rangle$  collapses the solution register to  $|\phi_{t+1}\rangle = \tilde{A}|\phi_t\rangle$ , and if postselection fails the state collapses to  $\tilde{I}|\phi_t\rangle \approx |\phi_t\rangle$  allowing the state to be reused for further computation. The accuracy to which  $\tilde{A}$  and  $\tilde{I}$  retain the structure of  $A$  and  $I$  will be discussed in the next section.

### III. ERROR ANALYSIS

The matrix  $A$  in Eq. (4) can be defined in terms of its diagonals, where the main diagonal  $d_0 = 1$ ,  $d_1 = -r/2$  and  $d_{-1} = r/2$ . Similarly, the corresponding terms in  $\tilde{A}$  can be evaluated as a function of  $r$  and  $\theta$ . Considering a  $4 \times 4$  matrix to avoid unnecessary negligible terms,  $\tilde{A}$  can be expressed as

$$\begin{aligned} \tilde{A} = & \\ d_0 : & \frac{1}{2} \left( \sin(\theta) + \frac{\sin(\theta\sqrt{r^2+1})}{\sqrt{r^2+1}} \right) \\ d_1, -d_{-1} : & -\frac{r \sin(\theta\sqrt{r^2+1})}{2\sqrt{r^2+1}} \\ d_2, d_{-2} : & \frac{1}{2} \left( \sin(\theta) - \frac{\sin(\theta\sqrt{r^2+1})}{\sqrt{r^2+1}} \right) \end{aligned} \quad (9)$$

The similarity between the matrices in Eq. (4) and (9) can be compared by constructing a difference matrix that quantifies the error of the terms relative to the main diagonal. The property that Eq. (9) must satisfy is  $d_1, -d_{-1} = -rd_0/2$  with other elements equalling 0, i.e. the relative proportions of the matrix must be consistent. If Eq. (4) is scaled by  $d_0^{(\text{Eq.9})}$  to yield equal diagonal elements with Eq. (9), then subtracting Eq. (9) from the scaled Eq. (4) gives the difference matrix  $E_A$ , given by

$$\begin{aligned} E_A = & \\ d_0 : & 0 \\ d_1, -d_{-1} : & -\frac{r}{4} \left( \sin(\theta) - \frac{\sin(\theta\sqrt{r^2+1})}{\sqrt{r^2+1}} \right) \\ d_2, d_{-2} : & -\frac{1}{2} \left( \sin(\theta) - \frac{\sin(\theta\sqrt{r^2+1})}{\sqrt{r^2+1}} \right) \end{aligned} \quad (10)$$

The maximum error per time step can then be defined by taking the spectral norm of Eq. (10)

$$\|E_A\|_2 = \frac{1}{2} \left( \sin(\theta)\sqrt{r^2+1} - \sin(\theta\sqrt{r^2+1}) \right) \quad (11)$$

$$\approx \left( \frac{r^2\theta^3}{12} - \frac{r^2\theta^5}{120} + O(r^4\theta^5) \right) \sqrt{r^2+1} \quad (12)$$

equal to the largest singular value of the difference matrix. The leading-order approximation from the Taylor series expansion is provided in Eq. (12) to reveal that for the small values of  $r$  used in classical computations, the error per time step grows with  $O(r^2\theta^3)$ . The leading order terms in the individual expansions of  $\sin(\theta)\sqrt{r^2+1}$  and  $\sin(\theta\sqrt{r^2+1})$  are identical and thus cancel out in the subtraction, resulting in the high-order expression in Eq. (12). Since the number of time steps required can be expressed as  $T = \tau/r$  where  $\tau$  is the non-dimensional simulation time, the error per the simulation duration is

$$\epsilon/\tau = \frac{1}{2r} \left( \sin(\theta)\sqrt{r^2+1} - \sin(\theta\sqrt{r^2+1}) \right) \quad (13)$$

$$\approx \left( \frac{r\theta^3}{12} - \frac{r\theta^5}{120} + O(r^3\theta^5) \right) \sqrt{r^2+1} \quad (14)$$

This is comparable with the total error induced using the explicit Euler method, which is  $O(r^2)$  per time step and  $O(r)$  for the total simulation duration.

To demonstrate the advantageous properties of Eq. (13) and (14), the equivalent error for a different PDE, the heat equation, will be analysed for comparison. The heat equation features a second derivative term on the right-hand side

$$\frac{\partial\phi}{\partial t} = D \frac{\partial^2\phi}{\partial x_j \partial x_j} \quad (15)$$

where  $D$  is the diffusivity. Following the same discretisation procedure for a one-dimensional problem, the matrix  $A$  takes the form  $[d_{-1}, d_0, d_1] = [r_h, 1 - 2r_h, r_h]$  for the internal grid points, where  $r_h = D\Delta t/(\Delta x)^2$ . Following the same methodology, the leading order terms of the Taylor series expansion of the error for the heat equation are defined by the following piecewise function.

$$\epsilon_h/\tau = \begin{cases} \frac{2\theta^3}{3} - \frac{5r\theta^3}{3} + O(\theta^5) & \text{when } 0 < r \leq 1/3 \\ -\frac{2\theta^3}{3} + \frac{11r\theta^3}{3} + O(\theta^5) & \text{when } 1/3 < r \leq 1/2 \end{cases} \quad (16)$$

which shows that the leading order term is independent of  $r$  with a coefficient eight times larger than in Eq. (14) for the advection equation. This occurs because the leading-order terms do not cancel by subtraction as was demonstrated in the expansion for the advection equation in Eq. (12). This indicates that the structure of the heat equation matrix is not as closely maintained throughout the Hamiltonian evolution. Figure 1 visualises the growth of  $\epsilon/\tau$  for both the advection equation and the heat equation. For the advection equation, decreasing  $r$  linearly

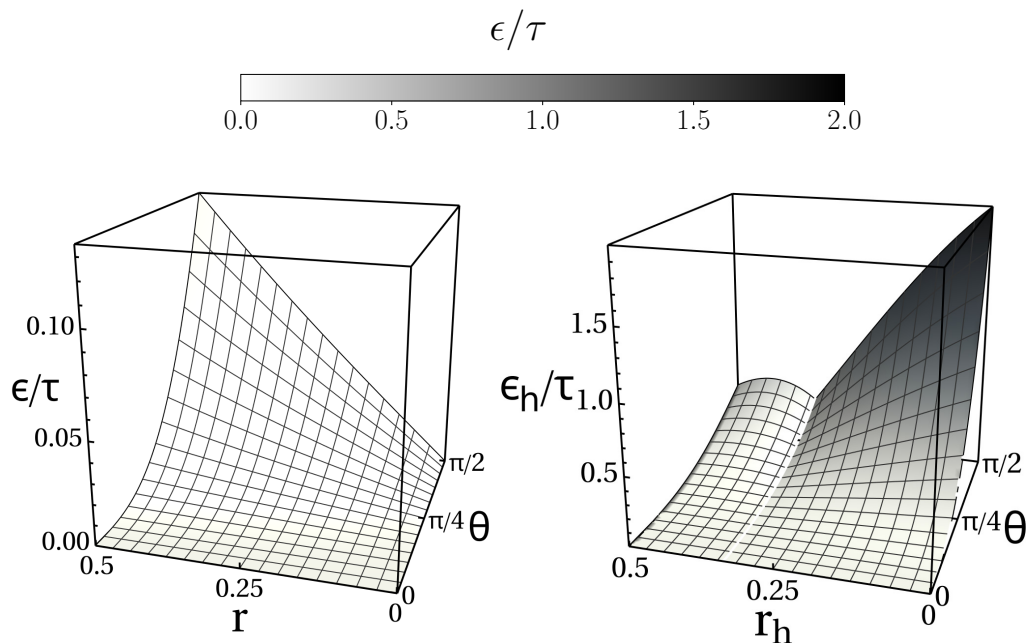


FIG. 1. Surface plot of the error per nondimensional simulation time as a function of  $r$  and  $\theta$  for the advection equation (left, defined in Eq. (13)) and the heat equation (right, Taylor series defined in Eq. (16)).

decreases the overall error in the quantum mechanical representation of the matrix. However, for the heat equation, the quantum mechanical error amplifies as  $r_h$  decreases, so reducing the error in the underlying scheme for numerical stability amplifies errors in the quantum mechanical representation. The differing growth in error with time step size for different PDEs, i.e.  $O(r)$  for the advection equation and  $O(1)$  for the heat equation demonstrates that the algorithm cannot be considered a sufficiently general PDE solver.

Figure 1 shows that reducing  $\theta$  reduces the error per successful time step, though this is at the cost of an increased number of unsuccessful time steps. The ability of the algorithm to withstand failed time steps and allowing the quantum state to be reused is dependent on the nature of  $\tilde{I}$  in Eq. (7). Following the same procedure,  $\tilde{I}$  can be written as

$$\begin{aligned} \tilde{I} = & \\ d_0 : & \frac{1}{2} \left( \cos(\theta) + \cos(\theta\sqrt{r^2+1}) \right) \\ d_{-1}, -d_1 : & 0 \\ d_2, d_{-2} : & \frac{1}{2} \left( \cos(\theta) - \cos(\theta\sqrt{r^2+1}) \right) \end{aligned} \quad (17)$$

and a difference matrix can be constructed that quantifies error relative to the main diagonal. Taking the spectral

norm of the difference matrix gives

$$\|E_I\|_2 = \frac{1}{2} \left( \cos(\theta) - \cos(\theta\sqrt{r^2+1}) \right) \quad (18)$$

$$= \frac{r^2\theta^2}{4} - \frac{r^2\theta^4}{24} + O(r^4\theta^4) \quad (19)$$

By contrast, the equivalent leading order term for the heat equation is  $2r\theta^2 + O(r^2\theta^2)$ . The high-order coupling for the advection equation between  $r$  and  $\theta$  demonstrates that the algorithm can withstand postselection failure when  $r$  is sufficiently small, allowing the computation to continue. On the other hand, for the heat equation, the error grows with a reduced order in  $r$  and again features a coefficient eight times larger, introducing prohibitively greater errors.

#### IV. TIME STEP SUCCESS PROBABILITY

The probability of a successful time step  $P = \|\tilde{A}|\phi\rangle\|^2$  can be studied by analysing the contribution of  $\tilde{I}$  to the state. The square of the spectral norm  $(\|\tilde{I}\|_2)^2$  corresponds to the largest action of  $\tilde{I}$  on a vector squared, so can be used to find the worst-case probability of successful measurement  $P_{\min} = 1 - (\|\tilde{I}\|_2)^2$ . Using the definition

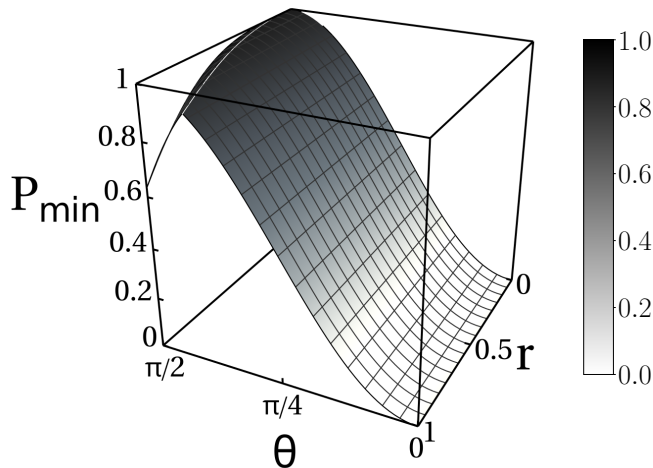


FIG. 2. Surface plot of the minimum probability of a successful time step defined in Eq. (20).

of  $\tilde{I}$  in Eq. (17),  $P_{\min}$  is defined as

$$P_{\min} = \begin{cases} \sin^2(\theta) & \text{when } 0 \leq \theta < \frac{\pi}{1+\sqrt{r^2+1}} \\ \sin^2(\theta\sqrt{r^2+1}) & \text{when } \frac{\pi}{1+\sqrt{r^2+1}} \leq \theta \leq \frac{\pi}{2} \end{cases} \quad (20)$$

which is visualised in Fig. 2. The figure shows that  $P_{\min}$  is optimal for small values of  $r$  and when  $\theta = \pi/(1+\sqrt{r^2+1})$ , approaching unity as  $r$  approaches zero. Using this value of  $\theta$  for a typical case where  $r = 0.1$ , the minimum probability  $P_{\min} = 99.9985\%$ , corresponding to a worst case of 67 000 successful time steps per failed time step on average.

It is shown in Section VI that for a practical configuration, the probability of postselection success is mostly represented by  $\sin^2(\theta)$  for the configuration tested, with the contribution from  $\sin^2(\theta\sqrt{r^2+1})$  having a reduced role leading to  $\theta = \pi/2$  being optimal in practice. For example,  $r = 0.1$  and  $\theta = \pi/2$  resulted in over 39 million successful time steps for every failed time step.

## V. COMPLEXITY ANALYSIS

The number of qubits grows as  $n = O(\log N)$  since the computational grid is compressed into the amplitudes of the exponentially growing computational basis states. The CFL condition  $r_{\max} = u_{j,\max}\Delta t/\Delta x < 1$  governs the time step size, and therefore the number of time steps and the required circuit depth. For three-dimensional problems,  $N$  must increase eight-fold to halve  $\Delta x$  and therefore halve  $\Delta t$ , which results in the number of time steps growing with  $N^{1/3}$ , or  $N^{1/D}$  in  $D$ -dimensional space. If the Hamiltonian evolution time  $\theta$  is chosen to be  $\pi/2$  where a time step succeeds with near certainty (see Section IV), then the circuit depth also grows as  $N^{1/D}$ . In terms of error, Eq. (14) shows that  $\epsilon$  grows linearly with  $r$  for the entire simulation, so the circuit depth grows with

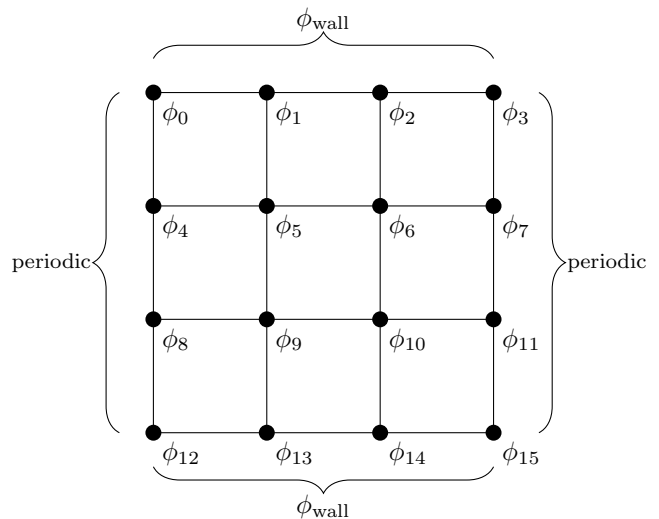


FIG. 3. Schematic of the computational domain for a channel flow with  $4^2$  cells.

$1/\epsilon$ . Considering the sparse Hamiltonian simulation algorithm of Berry *et al.* [27], the gate requirements of the Hamiltonian simulation grow with

$$O\left(\zeta\left(n + \log^{5/2}(\zeta/\epsilon)\right) \frac{\log(\zeta/\epsilon)}{\log\log(\zeta/\epsilon)}\right) \quad (21)$$

where  $\epsilon$  is the desired accuracy,  $\zeta = s\|H\|_{\max}\theta$ ,  $s$  is the sparsity, and  $\|H\|_{\max}\theta$  is the maximum value of the matrix  $H\theta$  which is  $O(1)$ . The sparsity of the Hamiltonian  $H$  is equal to the sparsity of  $A$ , which is  $s = 1 + Dk$ , where  $k$  is the order of the spatial discretisation. The complexity of the Hamiltonian simulation step can therefore be written as

$$O\left(Dk\left(\log(N) + \log^{5/2}(Dk/\epsilon)\right) \frac{\log(Dk/\epsilon)}{\log\log(Dk/\epsilon)}\right) \quad (22)$$

Suppressing the polylogarithmic terms for simplicity, this reduces to  $\tilde{O}(Dk)$ , revealing that the dominant source of error arises from the encoding of the nonunitary operator and the explicit Euler method rather than the Hamiltonian simulation. Combining all of these contributions, the circuit depth grows as  $\tilde{O}(N^{1/3}k/\epsilon)$  for three-dimensional simulations or  $\tilde{O}(N^{1/D}Dk/\epsilon)$  for  $D$ -dimensional simulations, suppressing the polylogarithmic terms from the Hamiltonian simulation.

## VI. SIMULATIONS

This section presents quantum statevector simulations of the algorithm applied to a two-dimensional laminar channel flow problem. The simulations do not account for noise or decoherence to provide an idealised representation of the algorithm, demonstrating its baseline capabilities. In all simulations, an  $N = 32^2 = 1024$  grid has

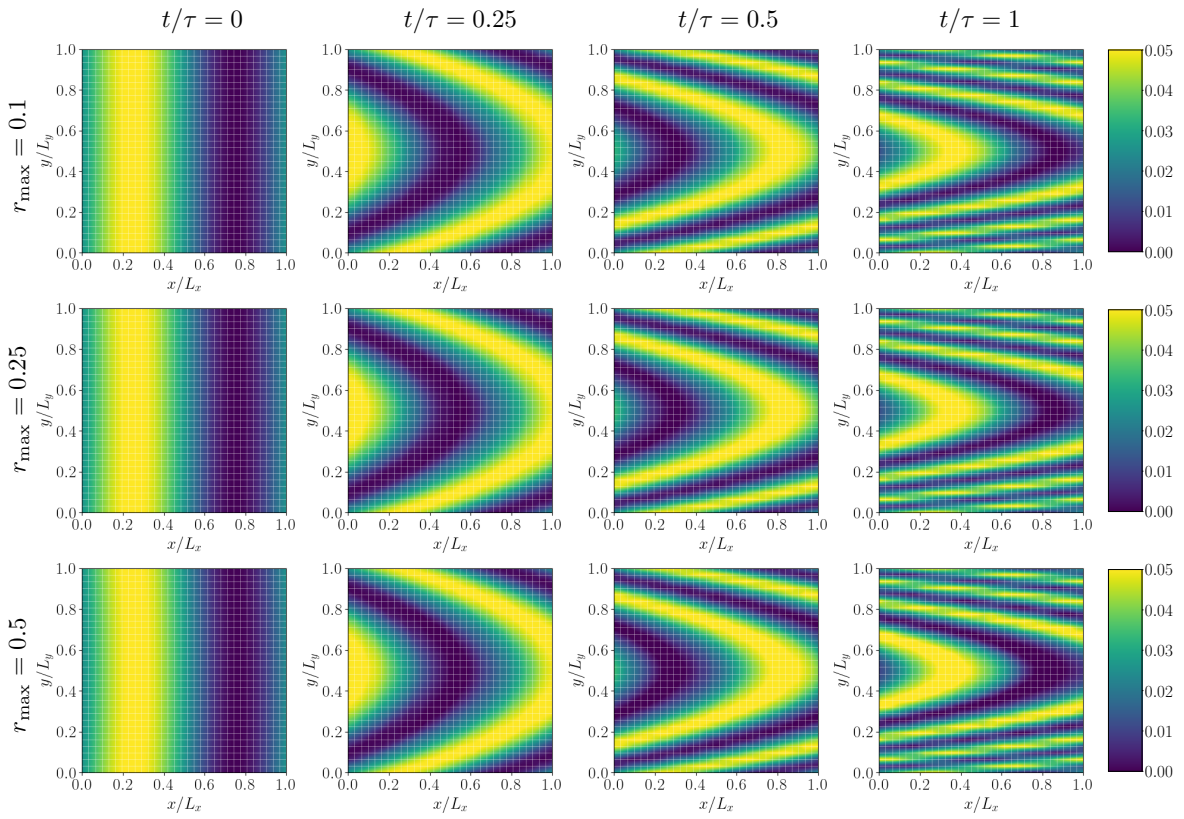
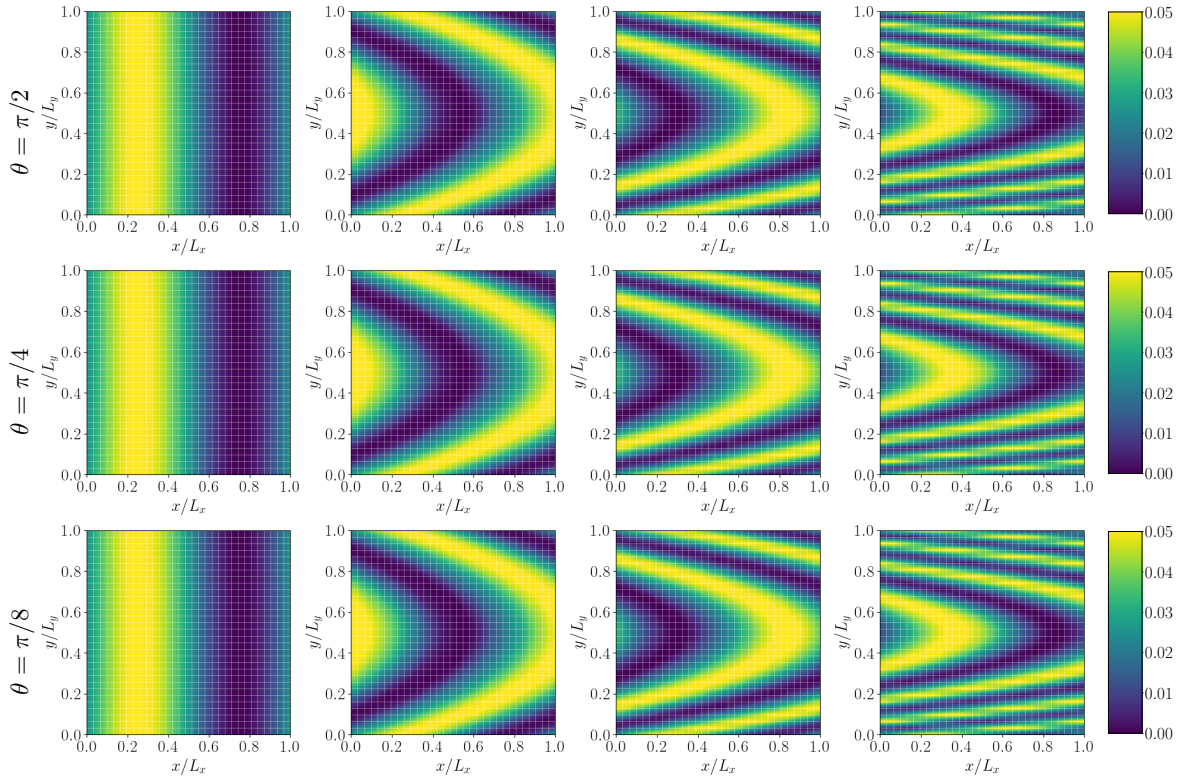
(a) Varying  $r$  for  $\theta = \pi/(1 + \sqrt{1+r_{\max}^2})$ (b) Varying  $\theta$  for  $r_{\max} = 0.25$ 

FIG. 4. Evolution of the quantum amplitudes from statevector simulations of a 2D laminar channel flow described by the advection equation at different time intervals. The  $32^2$  computational grid is superimposed.

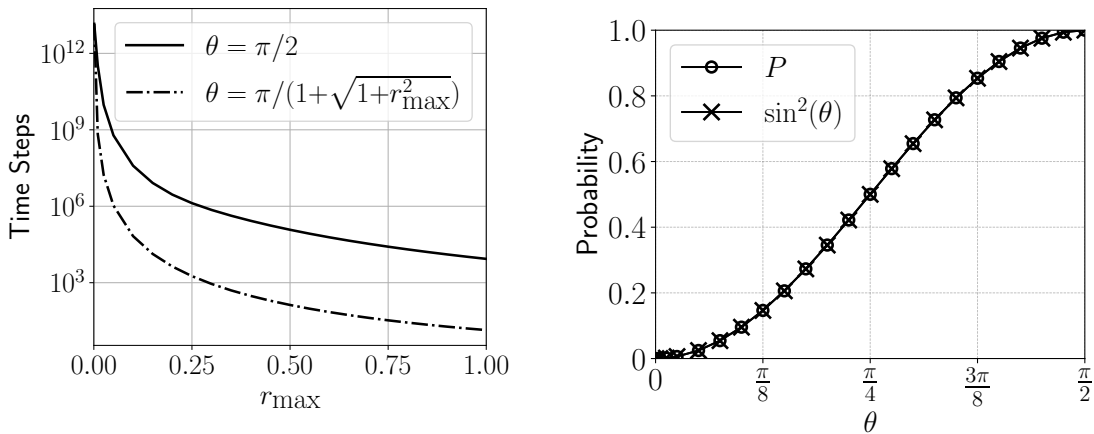


FIG. 5. The typical number of successful time steps for every failed time step as a function of  $r_{\max}$  for different values of  $\theta$  (left), and the probability of a successful time step  $P = \|\tilde{A}|\phi_t\rangle\|^2$  and the prediction  $\sin^2(\theta)$  for the  $r_{\max} = 0.25$  case (right).

been used that corresponds to 10 qubits representing the solution and the additional ancilla qubit required by the algorithm. The simulations use a fourth-order central FDM for the internal grid points, reducing to second-order towards the non-periodic boundaries.

A schematic of the computational domain for 16 grid points is shown in Fig. 3. The velocity field  $\vec{u} = [u, v]$  is described by the analytical solution to the Navier-Stokes equations in this configuration, known as a Plane Poiseuille flow, which has a parabolic profile of  $u$  in the vertical direction leading to the nondimensional CFL parameter to be defined as

$$r(y) = \frac{u(y)\Delta t}{\Delta x} \quad (23)$$

$$= r_{\max}(4y(1-y)) \quad 0 \leq y \leq 1 \quad (24)$$

which varies from 0 at the walls to  $r_{\max}$  at the centre of the domain, where  $y$  is the vertical normalised distance. The vertical component of the velocity  $v = 0$  because the flow is laminar. The scalar  $\phi$  is initialised as a sine wave in the horizontal direction as

$$\phi(x) = \sin(2\pi x), \quad 0 \leq x \leq 1 \quad (25)$$

where  $x$  is the corresponding normalised horizontal distance. The  $x$  boundaries are periodic, so fluid that flows out of the right boundary enters through the left boundary. Dirichlet boundary conditions are employed for the top and bottom boundaries where the value of  $\phi_{\text{wall}}$  is specified according to Eq. (25) to maintain the initial conditions, i.e. a no-slip wall. This boundary specification results in a single entry of 1 on the diagonal of matrix  $A$  for cells corresponding to the Dirichlet boundary.

The evolution of the quantum amplitudes with time for (a) varying CFL parameter  $r$  and (b) varying Hamiltonian evolution time  $\theta$  from the statevector simulations is shown in Fig. 4. The quantum amplitudes have been reconstructed into a grid for the ease of data visualisation. The equivalent simulation time corresponds to

1000 successful time steps for  $r_{\max} = 0.1$ , 400 successful time steps for  $r_{\max} = 0.25$  and 200 successful time steps for  $r_{\max} = 0.5$ . The simulations in Fig. 4a use  $\theta = \pi/(1 + \sqrt{r_{\max}^2 + 1})$  calculated from Fig. 2 to optimise  $P_{\min}$ , i.e. the worst-case probability of measurement success. The simulations in 4b use a constant  $r_{\max} = 0.25$  while varying  $\theta$  to  $\pi/2$ ,  $\pi/4$  and  $\pi/8$ . Varying  $\theta$  alters the probability of a successful time step  $P = \|\tilde{A}|\phi_t\rangle\|^2$ , and information about  $P$  is presented in Fig. 5 for this configuration. The value of  $\theta$  that optimises the worst-case  $P_{\min}$  is not found to be optimal in practice, with  $\pi/2$  providing a significantly greater probability of postselection success. For example, when  $r_{\max} = 0.1$ ,  $\theta = \pi/(1 + \sqrt{r_{\max}^2 + 1})$  leads to a typical 67 000 successful time steps for every unsuccessful time step compared to over 39 million when  $\theta = \pi/2$ . The prediction of  $\sin^2(\theta)$  from Fig. 2 is very accurate for all values of  $\theta$  as shown in Fig. 5. Although the probability of a time step success is close to certain when  $\theta = \pi/2$ , there remains a small chance of failure so the algorithm cannot be considered deterministic. The  $\theta = \pi/4$  and  $\pi/8$  cases in Fig. 4b demonstrate the ability of the algorithm to withstand postselection failure.

Figure 4 shows a consistent solution is reached regardless of the parameters tested, and this closely corresponds to the classical solution as shown by the error map in Fig. 6. The classical computations were performed by iteratively applying the matrix  $A$  directly to the solution vector, as shown in Eq. (3). The error is shown as a percentage calculated by  $100|\vec{\phi}/\|\vec{\phi}\| - |\phi|/\max(\vec{\phi})|$ . In all cases, the classical solution is normalised by  $\|\vec{\phi}\|$  so the quantum and classical solutions can be readily compared. The error map shows that the errors remain small after the simulation for every case. Figure 6 shows that when  $r_{\max} = 0.1$ , the difference between the quantum and classical solution mostly remains under 1%, and these errors grow linearly with increasing  $r_{\max}$ . Figure 6b shows how the errors vary with  $\theta$  under the influence of unsuccessful time steps. Reducing  $\theta$  does not influence the accuracy

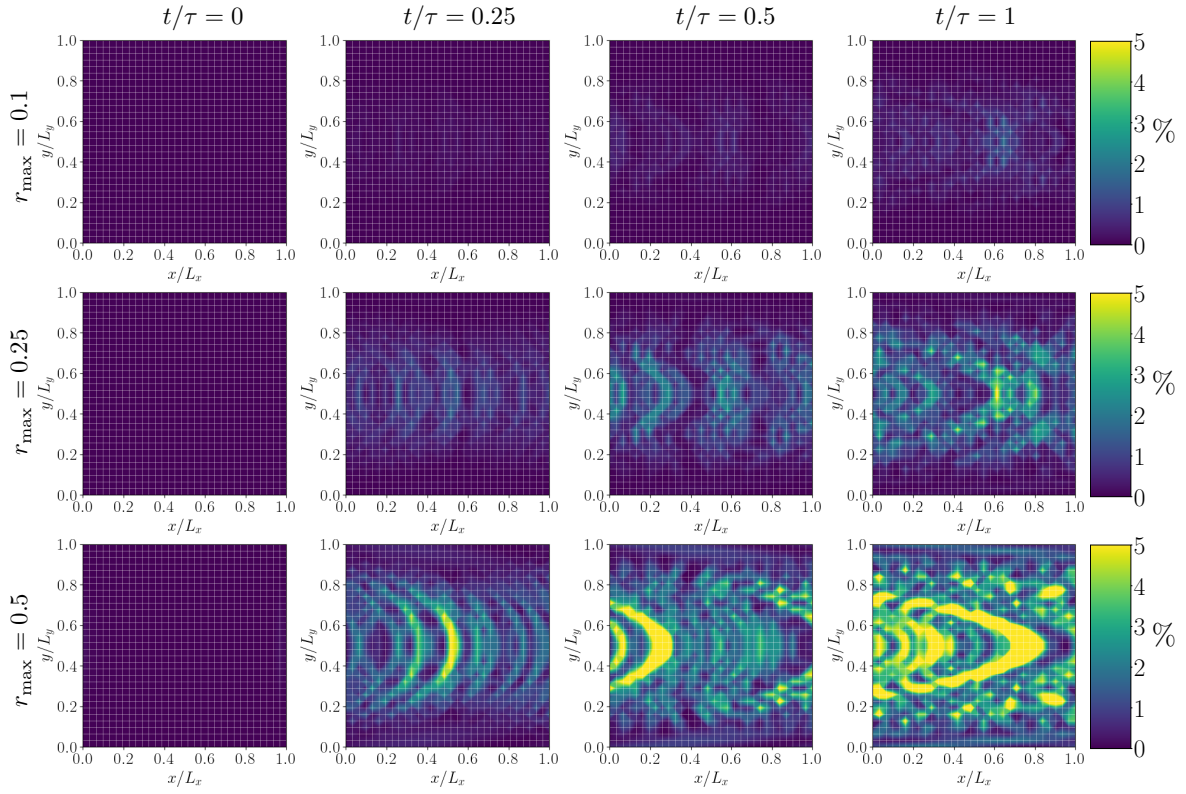
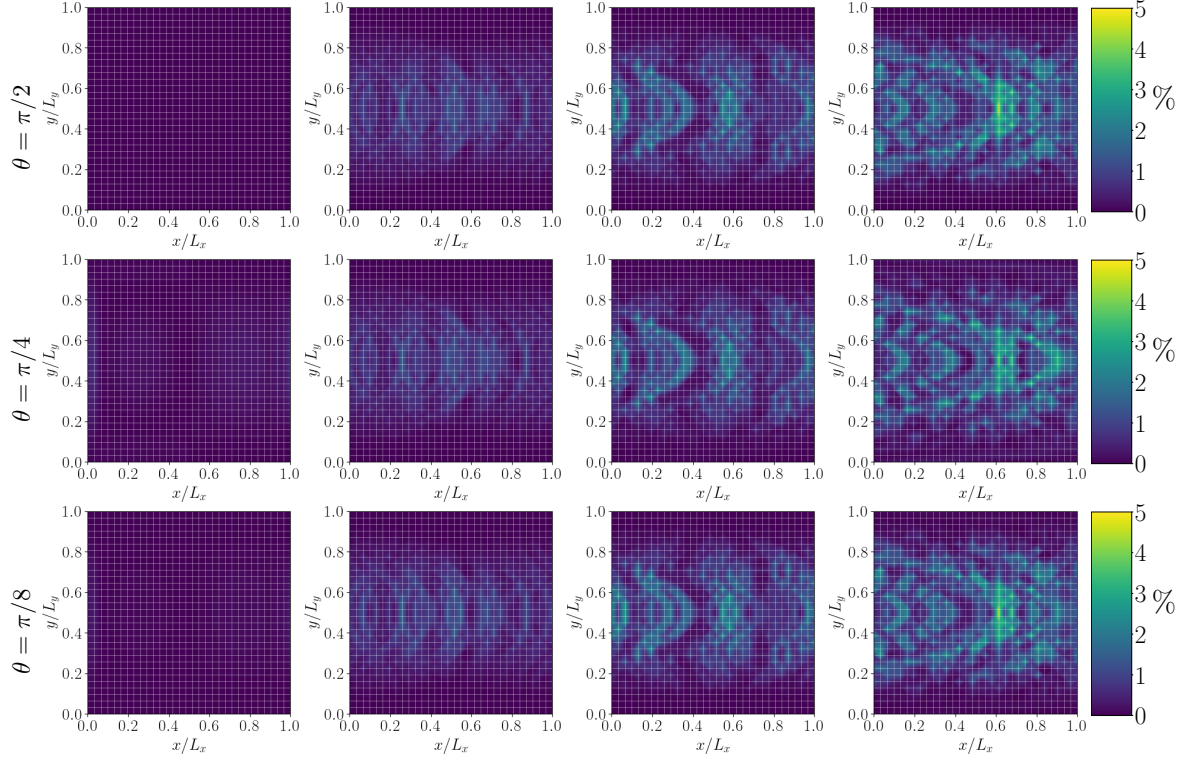
(a) Varying  $r$  for  $\theta = \pi/(1 + \sqrt{1+r_{\max}^2})$ (b) Varying  $\theta$  for  $r_{\max} = 0.25$ 

FIG. 6. Contours of the error compared to corresponding classical computations as a percentage, defined as  $100|\vec{\phi}/|\vec{\phi}|| - |\phi|/|\max(\vec{\phi})|$ . The  $32^2$  computational grid is superimposed.



of the overall solution, but does require more time steps to be attempted, thereby reducing the efficiency of the algorithm. As a result,  $\theta = \pi/2$  is the most efficient configuration. In all cases, the errors accumulate towards the centre of the domain where the velocity is greatest. The error map displays the parabolic profiles of the scalar field rather than random noise, indicating that the errors are susceptible to features of the flow. The algorithm accurately represents the Dirichlet boundary treatment where the scalar gradients are greatest, as demonstrated by the errors reducing to zero towards the boundaries.

## VII. CONCLUSIONS

This paper presented a quantum algorithm for solving the advection equation, a linear PDE prevalent in various scientific and engineering industries. The core of the algorithm uses sparse Hamiltonian simulation where the matrix  $A$  arising from the explicit FDM was embedded within a Hamiltonian  $H$  to advance the solution in time. The resulting unitary operator  $U = e^{-iH\theta}$  retains  $A$  to a high accuracy even for large values of  $\theta$ , thus ensuring that a time step was completed with a high probability. In instances where postselection failed, the resulting operation closely approximated the identity matrix, minimising the impact on the quantum state and allowing the computation to be continued.

From a resource utilisation perspective, qubit requirements grow logarithmically with the number of grid points  $N$  and gate requirements grow polynomially as  $\tilde{O}(N^{1/D}Dk/\epsilon)$ . This represents a significant improvement in complexity compared to classical methods, which typically exhibit a scaling of  $O(N^{(1+D)/D})$ .

The derived mathematical expressions for the error for successful and unsuccessful time steps in terms of  $r$

demonstrated a quadratic  $O(r^2)$  scaling per time step and linear  $O(r)$  for the simulation duration. This did not universally apply to all PDEs, as was demonstrated by the reduction in order for the heat equation, where the leading order term was independent of  $r$ , i.e.  $O(1)$ . Consequently, the numerical scheme for the advection equation can be accurately represented on a quantum computer using this method, but this does not necessarily apply to other PDEs.

The potential of the algorithm was demonstrated through two-dimensional simulations of a scalar transported in a laminar channel flow with fourth-order spatial discretisation. The quantum state evolved according to the advection equation and the amplitudes closely agreed with equivalent classical computations for all parameters tested.

Next, conducting simulations that mimic real, noisy quantum hardware is important to assess the algorithm's performance in a realistic quantum computing environment, ascertaining the quality of qubits required for a quantum advantage. The algorithm was presented in the context of solving the advection equation, although the methodology may extend to a wider range of problems, requiring interdisciplinary collaborations to investigate. Developing algorithms that encode the solution of a PDE in a quantum state is only a step towards achieving a practical quantum advantage, with methods for efficiently preparing initial conditions and extracting useful global statistics from these states being crucial for preparing the engineering industry to be quantum-ready.

## ACKNOWLEDGMENTS

This research was funded by the Engineering and Physical Sciences Research Council in the United Kingdom, grant number EP/W032643/1.

- 
- [1] S. Bravyi, O. Dial, J. M. Gambetta, D. Gil, and Z. Nazario, The future of quantum computing with superconducting qubits, *Journal of Applied Physics* **132** (2022), 160902.
  - [2] L. J. Stephenson, D. P. Nadlinger, B. C. Nichol, S. An, P. Drmota, T. G. Ballance, K. Thirumalai, J. F. Goodwin, D. M. Lucas, and C. J. Ballance, High-rate, high-fidelity entanglement of qubits across an elementary quantum network, *Physical Review Letters* **124** (2020), 110501.
  - [3] Y. Cao, A. Papageorgiou, I. Petras, J. Traub, and S. Kais, Quantum algorithm and circuit design solving the Poisson equation, *New Journal of Physics* **15** (2013), 013021.
  - [4] P. C. Costa, S. Jordan, and A. Ostrander, Quantum algorithm for simulating the wave equation, *Physical Review A* **99** (2019), 012323.
  - [5] S. Wang, Z. Wang, W. Li, L. Fan, Z. Wei, and Y. Gu, Quantum fast Poisson solver: the algorithm and complete and modular circuit design, *Quantum Information Processing* **19**, 1 (2020).
  - [6] A. M. Childs, J.-P. Liu, and A. Ostrander, High-precision quantum algorithms for partial differential equations, *Quantum* **5** (2021), 574.
  - [7] B. D. Clader, B. C. Jacobs, and C. R. Sprouse, Preconditioned quantum linear system algorithm, *Physical Review Letters* **110** (2013), 250504.
  - [8] A. Montanaro and S. Pallister, Quantum algorithms and the finite element method, *Physical Review A* **93** (2016), 032324.
  - [9] A. M. Childs and J.-P. Liu, Quantum spectral methods for differential equations, *Communications in Mathematical Physics* **375**, 1427 (2020).
  - [10] S. Lloyd, G. De Palma, C. Gokler, B. Kiani, Z.-W. Liu, M. Marvian, F. Tennie, and T. Palmer, Quantum algorithm for nonlinear differential equations, *arXiv Preprint* (2020), 2011.06571.
  - [11] J.-P. Liu, H. Ø. Kolden, H. K. Krovi, N. F. Loureiro, K. Trivisa, and A. M. Childs, Efficient quantum al-

- gorithm for dissipative nonlinear differential equations, *Proceedings of the National Academy of Sciences* **118**, e2026805118 (2021).
- [12] A. Peruzzo, J. McClean, P. Shadbolt, M.-H. Yung, X.-Q. Zhou, P. J. Love, A. Aspuru-Guzik, and J. L. O’Brien, A variational eigenvalue solver on a photonic quantum processor, *Nature communications* **5** (2014), 4213.
- [13] M. Lubasch, J. Joo, P. Moinier, M. Kiffner, and D. Jaksch, Variational quantum algorithms for nonlinear problems, *Physical Review A* **101** (2020), 010301.
- [14] O. Kyriienko, A. E. Paine, and V. E. Elfving, Solving nonlinear differential equations with differentiable quantum circuits, *Physical Review A* **103** (2021), 052416.
- [15] D. Jaksch, P. Givi, A. J. Daley, and T. Rung, Variational quantum algorithms for computational fluid dynamics, *AIAA Journal* **61**, 1885 (2023).
- [16] N. Gourianov, M. Lubasch, S. Dolgov, Q. Y. van den Berg, H. Babae, P. Givi, M. Kiffner, and D. Jaksch, A quantum-inspired approach to exploit turbulence structures, *Nature Computational Science* **2**, 30 (2022).
- [17] D. W. Berry, High-order quantum algorithm for solving linear differential equations, *Journal of Physics A: Mathematical and Theoretical* **47** (2014), 105301.
- [18] D. W. Berry, A. M. Childs, A. Ostrander, and G. Wang, Quantum algorithm for linear differential equations with exponentially improved dependence on precision, *Communications in Mathematical Physics* **356**, 1057 (2017).
- [19] J. M. Arrazola, T. Kalajdziewski, C. Weedbrook, and S. Lloyd, Quantum algorithm for nonhomogeneous linear partial differential equations, *Physical Review A* **100** (2019), 032306.
- [20] A. W. Harrow, A. Hassidim, and S. Lloyd, Quantum algorithm for linear systems of equations, *Physical Review Letters* **103**, 10.1103/PhysRevLett.103.150502 (2009), 150502.
- [21] A. M. Childs, R. Kothari, and R. D. Somma, Quantum algorithm for systems of linear equations with exponentially improved dependence on precision, *SIAM Journal on Computing* **46**, 1920 (2017).
- [22] A. Suau, G. Staffelbach, and H. Calandra, Practical quantum computing: Solving the wave equation using a quantum approach, *ACM Transactions on Quantum Computing* **2**, 1 (2021).
- [23] L. Budinski, Quantum algorithm for the advection–diffusion equation simulated with the lattice boltzmann method, *Quantum Information Processing* **20** (2021).
- [24] S. Jin, N. Liu, and Y. Yu, Quantum simulation of partial differential equations via schrodingerisation (2022), arXiv Preprint 2212.13969 (2022).
- [25] S. Jin, N. Liu, and Y. Yu, Quantum simulation of partial differential equations: Applications and detailed analysis, *Physical Review A* **108** (2023), 032603.
- [26] S. Jin, X. Li, N. Liu, and Y. Yu, Quantum simulation for partial differential equations with physical boundary or interface conditions, *Journal of Computational Physics* **498** (2024), 112707.
- [27] D. W. Berry, A. M. Childs, and R. Kothari, Hamiltonian simulation with nearly optimal dependence on all parameters, in *IEEE 56th Annual Symposium on Foundations of Computer Science* (2015) pp. 792–809.
- [28] R. M. Gingrich and C. P. Williams, Non-unitary probabilistic quantum computing, in *Proceedings of the Winter International Symposium on Information and Communication Technologies* (2004).
- [29] R. Courant, K. Friedrichs, and H. Lewy, Über die partiellen differenzgleichungen der mathematischen physik, *Mathematische Annalen* **100**, 32 (1928).